PAPER

Check for updates

MOF-derived nitrogen-doped porous carbon nanofibers with interconnected channels for high-stability Li⁺/Na⁺ battery anodes†

Kainian Chu, [ID] [ab] Mulin Hu,*[a] Bo Song,[a] Senlin Chen,[a] Junyu Li,[a] Fangcai Zheng, [ID] [b] Zhiqiang Li,[b] Rui Li [ID] [a] and Jingya Zhou[a]

Heteroatom-doped porous carbon materials have been widely used as anode materials for Li-ion and Na-ion batteries, however, improving the specific capacity and long-term cycling stability of ion batteries remains a major challenge. Here, we report a facile based metal–organic framework (MOFs) strategy to synthesize nitrogen-doped porous carbon nanofibers (NCNFs) with a large number of interconnected channels that can increase the contact area between the material and the electrolyte, shorten the diffusion distance between Li⁺/Na⁺ and the electrolyte, and relieve the volume expansion of the electrode material during cycling; the doping of nitrogen atoms can improve the conductivity and increase the active sites of the carbon material, can also affect the microstructure and electron distribution of the electrode material, thereby improving the electrochemical performance of the material. As expected, the obtained NCNFs-800 exhibited excellent electrochemical performance with high reversible capacity (for Li⁺ battery anodes: 1237 mA h g⁻¹ at 100 mA g⁻¹ after 200 cycles, for Na⁺ battery anodes: 323 mA h g⁻¹ at 100 mA g⁻¹ after 150 cycles) and long-term cycling stability (for Li⁺ battery anodes: 635 mA h g⁻¹ at 2 A g⁻¹ after 5000 cycles, for Na⁺ battery anodes: 194 mA h g⁻¹ at 2 A g⁻¹ after 5000 cycles).

1. Introduction

With global energy consumption, renewable energy has attracted public attention. Rechargeable alkali metal-ion batteries (such as lithium or sodium-ion batteries) with high energy and power density have been widely recognized as promising energy storage systems for portable electronic devices.[1,2] Currently, graphite with a theoretical capacity of only 372 mA h g⁻¹ is widely used as a commercial anode material for lithium-ion batteries (LIBs) and sodium-ion batteries (SIBs). The low theoretical specific capacity and slow diffusion kinetics limit the rapid development of the battery market. Currently, carbonaceous materials have been proved to be one of the most promising anodes.[3,4] Thus, it is necessary to explore excellent carbonaceous anode materials for high-performance Li-ion and Na-ion batteries.

Carbonaceous materials have the advantages of high electrical conductivity, low cost, and environmental friendliness. Carbonaceous materials with various morphologies and

structures have been extensively studied as anode materials for alkali metal ion batteries,[5–7] For example, Zheng *et al.* reported that nitrogen-doped porous carbonaceous materials as stable anode material for lithium-ion batteries exhibited a reversible capacity of 2132 mA h g⁻¹ at 100 mA g⁻¹ after 50 cycles.[8] Metal–organic frameworks (MOFs) are widely used as self-sacrificial templates for the synthesis of porous carbonaceous materials, and the resulting carbonaceous materials always inherit the porous structure of MOFs.[9–11] Unfortunately, the interlayer spacing of carbonaceous materials is too small to effectively store a large amount of Li⁺ or Na⁺. So far, one of the effective strategies to improve the lithium/sodium storage performance of carbonaceous materials is to increase the interlayer spacing of carbonaceous materials, adjusting more Li⁺/Na⁺ adsorption active sites to enhance the capacitive contribution of LIBs and SIBs.[12,13] Heteroatom doping (such as N, S, P, *etc.*) has recently been shown to be a good way to enhance the capacitive contribution of carbonaceous materials, thereby enhancing their Li⁺/Na⁺ storage performance.[14,15] For example, Wang *et al.* reported a phosphorus and oxygen dual-doped porous carbon spheres with enhanced reaction kinetics, which facilitates the fast transfer of K⁺ and exhibits a reversible capacity of 401 mA h g⁻¹ at 100 mA g⁻¹ and excellent cycling stability.[16] In addition, heteroatom-doped (N, S, P, *etc.*) porous carbons can also be easily obtained by carbonization of MOFs with heteroatom-containing ligands.[17–19] Today, a new catalytic

[a]Hefei Technology College, Hefei 230011, China. E-mail: hml@htc.edu.cn

[b]Institutes of Physical Science and Information Technology and Key Laboratory of Structure and Functional Regulation of Hybrid Materials of Ministry of Education, Anhui University, Hefei, 230601, China

† Electronic supplementary information (ESI) available. See DOI: https://doi.org/10.1039/d2ra08135k

strategy is optimized for the synthesis of porous carbonaceous materials, carbonized MOFs precursors release gaseous molecules (*e.g.* CO_2, H_2O, NO_2, *etc.*), forming transition metals (*e.g.* Ni, Mn, and Co, *etc.*) or transition metal oxides (*e.g.* NiO, MnO, and Co_3O_4, *etc.*) can be used as catalysts, which can induce a large number of nanoporous defects in carbonaceous materials, alleviate the volume expansion of electrode materials during cycling, and expand the contact area between electrolyte and active materials.[20,21] Moreover, after the removal of catalysts, provides additional active sites for Li^+/Na^+ adsorption, leaving many cavities interconnected by channels, shortening the diffusion distance of electrons and Li^+/Na^+ during cycling, thereby improving electrochemical performance.[22]

In this work, we adopted a MOFs-derived strategy to prepare nitrogen-doped porous carbon nanofibers (NCNFs). Carbonized MOFs precursors release gaseous molecules, and the resulting MnO nodes act as *in situ* catalysts, and the ligands contain a large amount of N element, which facilitates *in situ* N doping of the product. As a result, the interlayer spacing of carbon material was increased, additional active sites and many cavities interconnected by channels are generated in the final carbon material, which alleviates the volume expansion of the electrode material during cycling, expands the contact area between the electrolyte and the active material, and shortens the diffusion distance of electrons and Li^+/Na^+ during cycling process, thereby improves the electrochemical performance of the electrode material.

2. Experimental section

2.1 Material synthesis

All chemicals are of analytical grade and were directly used without any further purification. In a typical synthesis procedure for Mn–NTA, 1.2 g of $MnCl_2$ and 0.6 g nitrilotriacetic acid (NTA) were added to 30 ml of deionized water under agitated stirring. After stirred for 10 min, 10 ml of isopropyl alcohol was added to the above solution and stirred for 30 minutes to form transparent solution. The mixture solution was then transferred into a Teflon-lined autoclave (50 ml) and heated at 180 °C for 6 h. The Mn–NTA precipitates were collected by centrifugation and washed with ethanol for three times, and then dried at 60 °C for 12 h. The MnO@N–C was synthesized through direct carbonization of Mn–NTA precipitates at different temperatures (600, 700 and 800 °C) for 2 h with a heating rate of 10 °C min in N_2. The MnO@N–C were etched by 3 M HCl for 4 h, and the corresponding samples were denoted as NCNFs-600, NCNFs-700, and NCNFs-800, respectively.

2.2 Material characterization

The X-ray diffraction (XRD) patterns of all samples were determined with an X-ray diffractometer (SmartLab 9KW) equipped with Cu-Kα radiation ($\lambda = 0.154$ nm) over the 2θ range of 10–70°. The thermal behavior of Mn–NTA and MnO@N–C were investigated used TGA-5500 thermoanalyser under flowing N_2 and air with a heating rate of 10 °C min^{-1}, respectively. Scanning electron microscopy (SEM, JEOLJSM-6700 M) and transmission electron microscopy (TEM, Hitachi H-800) with a voltage of 200 kV were performed on all as-prepared samples to characterize their microstructures and morphologies. High resolution transmission electron microscopy (HRTEM, JEOL-2011) was further used to investigate the structure of the resulting NCNFs-800. The FTIR spectrum of Mn–NTA and NTA were recorded by Fourier transform infrared spectroscopy (Hyperion 2000). The specific surface area and pore structure of NCNFs were measured by using a sorption analyzer (ASAP 2460) at 77 K. X-ray photoelectron spectroscopy (XPS) results were collected by using an ESCALAB 250 X-ray photoelectron spectrometer. The degree of graphitization of NCNFs were characterized by Raman spectrometer (Via-Reflex/inVia-Reflex).

2.3 Electrochemical measurements

The as-prepared sample was examined as an anode material for lithium/sodium ion batteries. The electrochemical performance of NCNFs electrodes were evaluated using a CR2032 coin-type cell assembled in an argon-filled glove box (MBRAUN UNILAB PRO, SP (1800/780)). The homogeneous slurry for the working electrodes was prepared by mixing the as-prepared sample (80%), polyvinylidene difluoride (PVDF, 10%), and carbon black (10%) with the addition of *N*-methyl-2-pyrrolidone (NMP). Finally, the slurry was coated on the copper foil, which was further dried in a vacuum oven at 80 °C overnight. The metallic Li and Na were used as the counter electrodes for LIBs and SIBs, respectively. For LIBs, the electrolyte was 1 M $LiPF_6$ in a mixture of ethylene carbonate (EC) and diethyl carbonate (DEC) (1 : 1 in volume), and Celgard 2400 polypropylene film was used as the cell separator. For SIBs, the electrolyte was 1 M $NaPF_6$ in ethylene carbonate and diethyl carbonate (EC : DEC = 1 : 1 in volume) and glass fiber (GF/D) from Whatman was used as the separator. The electrochemical performance was tested by a galvanostatic charge/discharge technique on a battery testing system (Neware). Cyclic voltammetry (CV) curves were performed on a CHI760E electrochemical workstation.

3. Results and discussion

As shown in Scheme 1, the nitrogen-doped porous carbon nanofibers (denoted as NCNFs) were synthesized through MOFs-derived strategy. Firstly, Mn–NTA precipitates were synthesized by the coordination of Mn^{2+} and nitrilotriacetic acid in the solvothermal process. Secondly, the resulting MOFs were carbonized to form MnO@N–C in N_2 and then etched with acid to obtain NCNFs. In the process of calcining the precursor, MOFs precursors release gaseous molecules (*e.g.* CO_2, H_2O, NO_2), and the resulting MnO nodes act as *in situ* catalysts, resulting in the final product with additional active sites and many cavities interconnected by channels. Moreover, and the ligands contain a large amount of N element, which facilitates *in situ* N doping of the product. The interconnected channels can increase the contact area between the material and the electrolyte, shorten the diffusion distance between Li^+/Na^+ and the electrolyte, and relieve the volume expansion of the electrode material during cycling. The doping of nitrogen atoms can
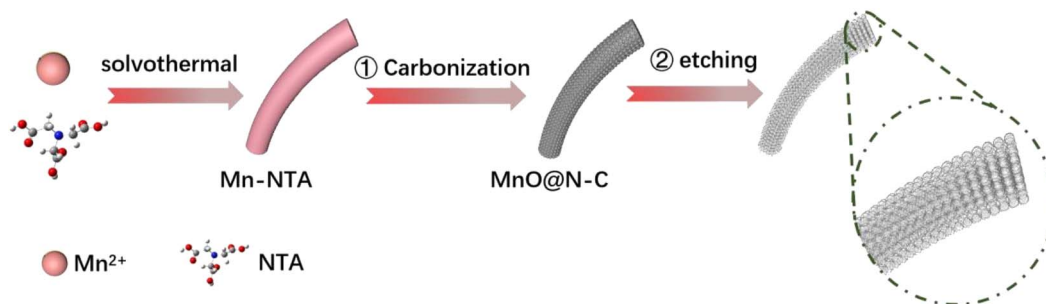
Scheme 1 Schematic illustration of the formation of NCNFs.

improve the conductivity, increase the active site and expand the interlayer spacing of the electrode material, and the introduction of non-carbon elements can also affect the microstructure and electron distribution of the electrode material, thereby changing the electrochemical properties of the material.[23–25]

The morphology of the resulting precursor (Mn–NTA nanofibers) was characterized by scanning electron microscopy (SEM) and transmission electron microscopy (TEM). The resulting precursor with smooth surface exhibits fiber-like structures with lengths of several micrometers and widths of approximately 150 nm (Fig. 1a and b). On the basis of the Fourier transform infrared spectroscopy (FTIR) spectrum

(Fig. S1†), the precursor can be indexed to Mn–NTA. Based on the TGA results (Fig. S2†), he precursor was carbonized in N_2 at temperatures of 600 °C, 700 °C, and 800 °C for 2 h. After carbonization of Mn–NTA in N_2, the product obtained without acid etching can be indexed to MnO@N–C (Fig. S3†), and the weight percentage of carbon in the MnO@N–C composite is 16.72% (Fig. S4†). As shown in Fig. S5,† the as-prepared MnO@N–C inherited the fiber-like morphology while the surface has become rough. In addition, MnO@N–C contains a large quantity of nanoparticles with a radius of approximately 5 nm. Then MnO@N–C was etched with acid to obtain NCNFs, the NCNFs inherited the nanofiber-like morphology of the precursor. Moreover, in the process of calcining the precursor,
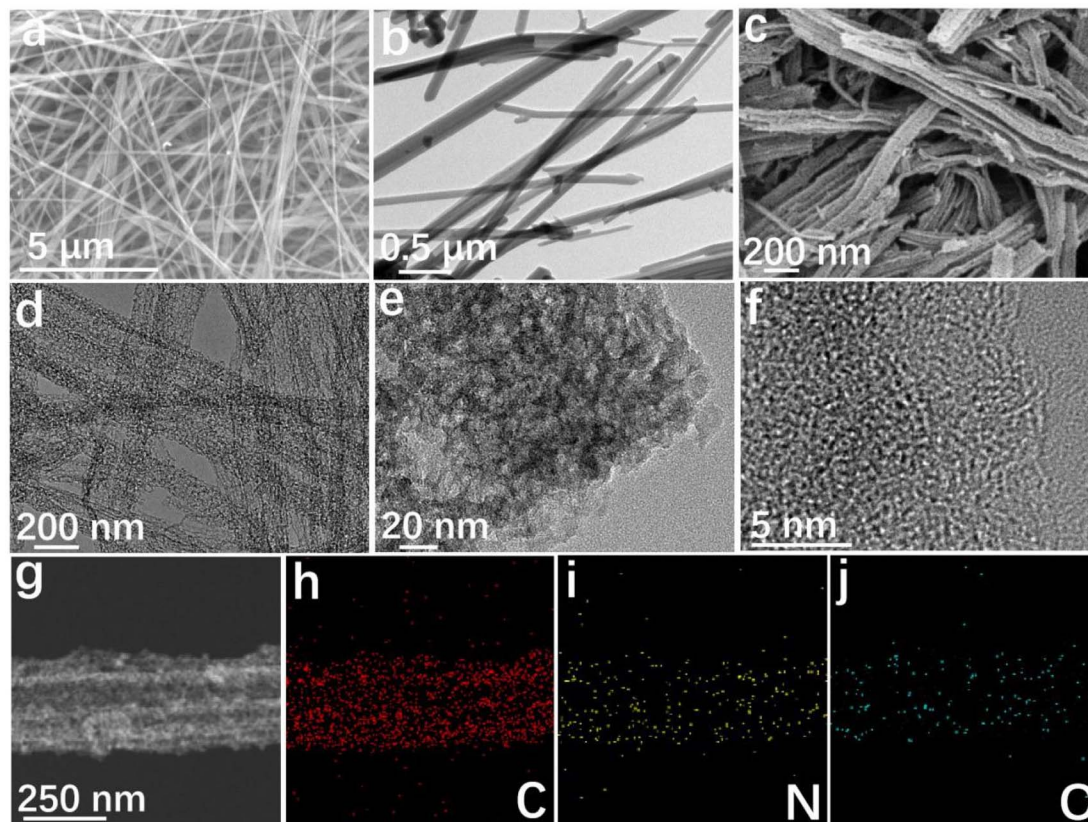

Fig. 1 Morphology and structure characterization of NCNFs-800. (a) SEM and (b) TEM images of Mn–NTA nanowires, (c) SEM, (d and e) TEM, (f) HRTEM and (g-j) EDS mapping images of NCNFs-800.

---

carbonization temperature, the content of N-Q and N-6 increase, while the contents of N-5 decrease, NCNFs contain a high nitrogen (N-6/N-5) ratio, which can induce defects and serve as electrochemically active sites for the adsorption of ions.[39]

The lithium-storage performances of NCNFs were investigated as anode materials for Li+ half cells. As shown in Fig. 3a, typical cyclic voltammetry (CV) curves of NCNFs-800 was tested at a scan rate of 0.1 mV s^{-1}, and it is seen that the first cycle is different from those of the subsequent ones and the intensity of all peaks drops significantly in comparison to the first cycle. Two broad cathodic peak at approximately 0.52 V and 1.42 V can be assigned to the interaction of Li+ with the surface active sites and generation of solid electrolyte interface (SEI) film.[40] The anodic peak at approximately 0.22 V can be attributed to the extraction of Li+ from NCNFs-800.[41] The CV curves overlap well after the subsequent ones, implying highly reversible Li+-storage performances.[42] As shown Fig. 3b, the galvanostatic discharge/charge (GCD) curves for NCNFs-800 at 0.1 A g^{-1} show that initial discharge/charge capacities of 1916 and 999 mA h g^{-1}, respectively, corresponding to an initial coulombic efficiency (ICE) of 52.15%. The GCD curves overlap well after the subsequent ones, implying highly reversible Li+-storage performances. The GCD profiles of NCNFs-600 and NCNFs-700 are shown in Fig. S12.† In addition, as shown in Fig. 3c, the cycling stability of NCNFs was further evaluated at a current density of 100 mA g^{-1}. The NCNFs-800 shows excellent cycling performance with a high discharge capacity of 1237 mA h g^{-1} after 200 cycles, which is superior than those of the NCNFs-700 (1055 mA h g^{-1}) and NCNFs-600 (919 mA h g^{-1}) and reported carbon anodes for LIBs (Table S2†). It was found that the specific capacity of NCNFs increased slowly after 10th cycle, which can be attributed to the activation of electrode materials during the cycling processes.[43] Meanwhile, the coulombic

efficiency (CE) of the NCNFs-800 is retained above 98.82% after the 200 cycles, suggesting that the NCNFs-800 has a good cyclic stability as an anode material in Li+ half cells. Fig. 3d shows the rate performances of NCNFs at different current densities. When the current density gradually increases from 100 to 200, 400, 600, 800 and 1000 mA g^{-1}, the specific capacities of NCNFs-800 decreases from 1150 to 1057, 894, 799, 760 and 716 mA h g^{-1}, respectively. When the current density decreased from 1000 to 100 mA g^{-1} again, the discharge capacity is retained at 1309 mA h g^{-1}, indicating that NCNFs-800 has good reversibility for LIBs. Moreover, the rate capability of NCNFs-800 is superior to those of NCNFs-600 and NCNFs-700. In addition, as shown in Fig. 3e, the long-term cyclic stability at a high current density of 2 A g^{-1} is also investigated. After 5000 cycles, it is surprisingly found that NCNFs-800 contain a high reversible capacity of 635 mA h g^{-1}, suggesting the excellent cycling performance, which is superior than NCNFs-600 and NCNFs-700 (Fig. S13†), implying its potential for practical applications. The cycling stabilities of NCNFs of 1 A g^{-1} is also shown in Fig. S14.†

The sodium-storage performances of NCNFs were investigated as anode materials for Na+ half cells. As shown in Fig. 4a, the initial three CV curves of NCNFs-800 at a scan rate of 0.1 mV s^{-1}, and it is seen that the first cycle is different from those of the subsequent ones. A broad peak at approximately 1.1 V appears in the first cathodic process, which can be attributed to the formation of SEI films.[44] In addition, the broad peak at approximately 0.25 V can be ascribed to the interaction of Na+ into the interlayer of carbon and the sorption of Na+ with active sites (defects and edge doping sites) in NCNFs-800.[45] The anodic peak at approximately 0.22 V can be attributed to the extraction of Na+ from NCNFs-800.[46] The CV curves overlap well after the subsequent ones, implying highly reversible Na+-storage performances.[47] As shown Fig. 3b, the galvanostatic discharge/
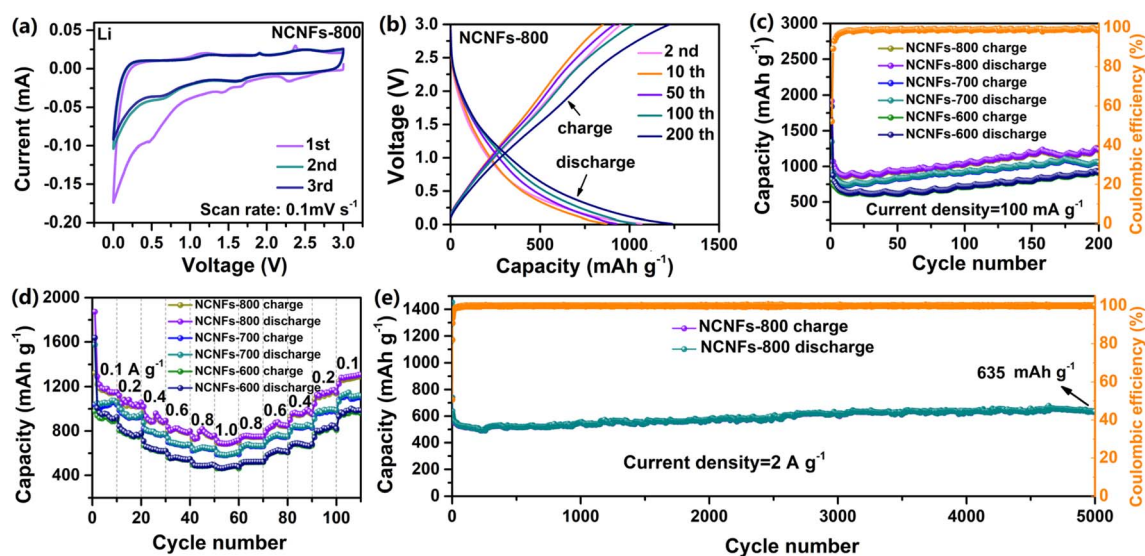

Fig. 3 The electrochemical performances of NCNFs in Li+ half cells. (a) CV curves of NCNFs-800 at 0.1 mV s^{-1}. (b) Discharge/charge profiles of NCNFs-800 at 0.1 A g^{-1}. (c) Cycling performances of NCNFs at 100 mA g^{-1}. (d) Rate capability of NCNFs at a current density from 0.1 to 10 A g^{-1}. (e) Cycling performance of NCNFs-800 at 2 A g^{-1}.
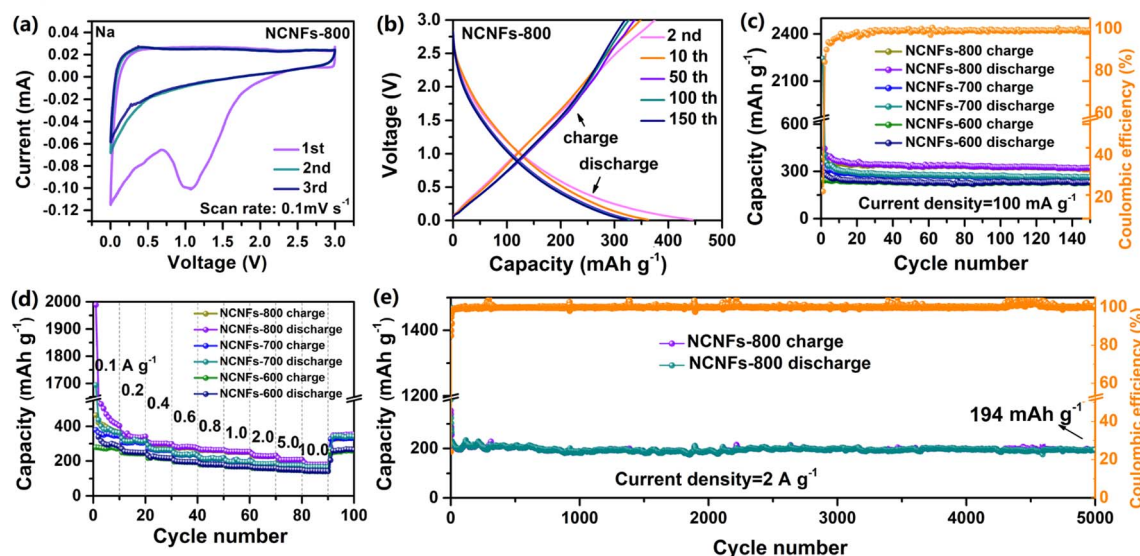
Fig. 4 The electrochemical performances of NCNFs in Na$^+$ half cells. (a) CV curves of NCNFs-800 at 0.1 mV s^{-1}. (b) Discharge/charge profiles of NCNFs-800 at 0.1 A g^{-1}. (c) Cycling performances of NCNFs at 100 mA g^{-1}. (d) Rate capability of NCNFs at a current density from 0.1 to 10 A g^{-1}. (e) Cycling performance of NCNFs-800 at 2 A g^{-1}.

charge (GCD) curves for NCNFs-800 at 0.1 A g^{-1} show that initial discharge/charge capacities of 1690 and 387 mA h g^{-1}, respectively, corresponding to an initial coulombic efficiency (ICE) of 22.93%, the low initial CE was mainly caused by the decomposition of the electrolyte and formation of SEI films,[48] and the low ICE is frequently obtained for porous carbon materials.[49] The GCD profiles of NCNFs-600 and NCNFs-700 are shown in Fig. S15.† In addition, as shown in Fig. 4c, the cycling stability of NCNFs was further evaluated at a current density of 100 mA g^{-1}. The NCNFs-800 shows excellent cycling performance with a high discharge capacity of 323 mA h g^{-1} after 150 cycles, which is superior than those of the NCNFs-700 (265 mA h g^{-1}) and NCNFs-600 (230 mA h g^{-1}) and reported carbon anodes for SIBs (Table S3†). Meanwhile, the coulombic efficiency (CE) of the NCNFs-800 is retained above 99.35% after the 150 cycles, suggesting that the NCNFs-800 has a good cyclic stability as an anode material in Na$^+$ half cells. Fig. 4d shows the rate performances of NCNFs at different current densities. When the current density gradually increases from 0.1 to 0.2, 0.4, 0.6, 0.8, 1.0, 2.0, 5.0 and 10.0 A g^{-1}, the specific capacities of NCNFs-800 decreases from 405 to 341, 299, 274, 264, 253, 231, 207 and 180 mA h g^{-1}, respectively. When the current density decreased from 10.0 to 0.1 mA g^{-1} again, the discharge capacity is retained at 356 mA h g^{-1}, indicating that NCNFs-800 has good reversibility for SIBs. Moreover, the rate capability of NCNFs-800 is superior to those of NCNFs-600 and NCNFs-700. In addition, as shown in Fig. 3e, the long-term cyclic stability at a high current density of 2 A g^{-1} is also investigated. After 5000 cycles, it is surprisingly found that NCNFs-800 contain a high reversible capacity of 194 mA h g^{-1}, suggesting the excellent cycling performance, which is superior than NCNFs-600 and NCNFs-700 (Fig. S16†), implying its potential for practical applications. The cycling stabilities of NCNFs of 1 A g^{-1} is also shown

in Fig. S17.† The high specific capacity and outstanding long-term cycling stability of NCNFs-800 could be attributed to its porous structure and interconnected channels and the doping of nitrogen atoms. The interconnected channels and porous structure can increase the contact area between the material and the electrolyte, shorten the Li$^+$/Na$^+$ diffusion distance, and relieve the volume expansion of the electrode material during cycling. The doping of nitrogen atoms can improve the conductivity of the electrode material and increase active sites.

In order to further explore the electrochemical reactions of NCNFs-800, we simply analyzed the lithium-storage and sodium-storage kinetics of NCNFs-800 based on the measured CV curves at different scan rates from 0.2 mV s^{-1} to 3.6 mV s^{-1} were shown in Fig. S18a and c.† The curves of NCNFs-800 are similar, and the peak intensities of the cathode and anode increase with the scan rate.[50] According the electrochemical theory, the current (i) is related to the scan rate (v):[51,52]

$$i = av^b \qquad (1)$$

$$\log(i) = b\log(v) + \log(a) \qquad (2)$$

where a and b are adjustable constants. The lithium-storage and sodium-storage mechanism of NCNFs-800 can be confirmed by b-value that can be obtained through the slope of $\log(i)$–$\log(v)$ fit curve. In general, the b-value closes to 0.5, implying that the electrochemical reaction is controlled by the diffusion-controlled process; while the b-value approaches to 1, indicating the ideal capacitive process.[53] As shown in Fig. S18b and d,† for lithium-storage and sodium-storage, the calculated b-values for NCNFs-800 of both cathodic and anodic perks are closed to 1.0, indicating that the lithium-storage and sodium-storage behavior for NCNFs-800 is dominated by a capacitive-
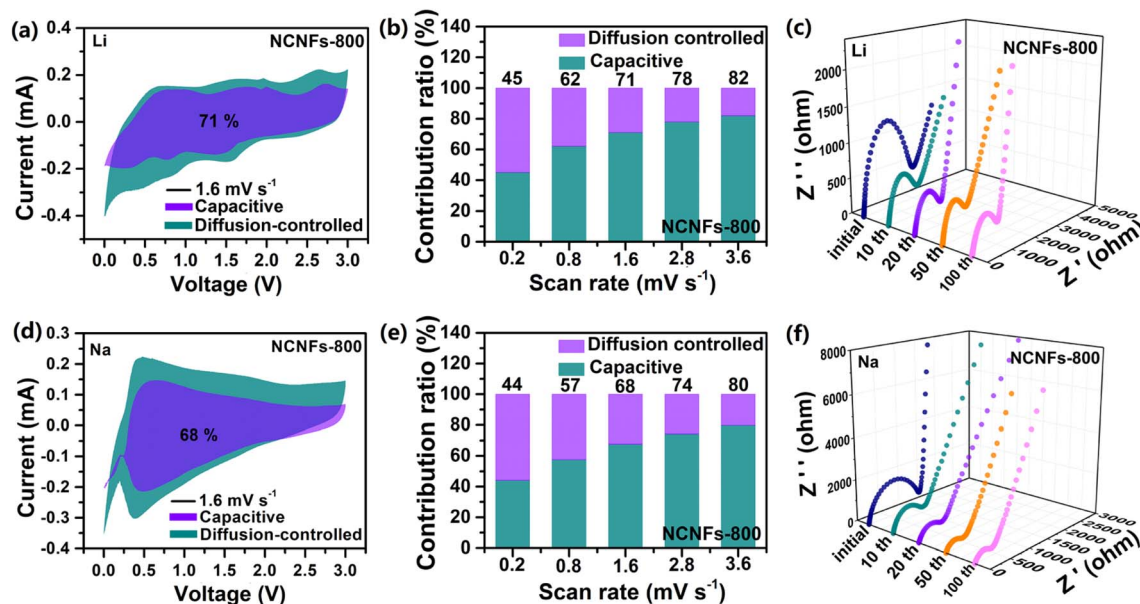
Fig. 5 Kinetics analysis of NCNFs. (a and d) Capacitive charge-storage contribution in the NCNFs-800 at a scan rate of 1.6 mV s^{-1} of LIBs and SIBs, respectively. (b and e) Contribution ratios of the capacitive process in the NCNFs-800 at different scan rates of LIBs and SIBs, respectively. (c and f) EIS curves of NCNFs-800 at different cycles of LIBs and SIBs, respectively.

controlled process. In addition, the capacitance contribution ratio can be calculated by the following formulas:[54,55]

$$i = k_1 v + k_2 v^{1/2} \tag{3}$$

$$i/v^{1/2} = k_1 v^{1/2} + k_2 \tag{4}$$

where $k_1 v$ represents the contribution of the capacitive process, At the scan rate of 1.6 mV s^{-1}, the capacitive contribution of lithium-storage and sodium-storage for NCNFs-800 are approximately 71% and 68%, respectively (Fig. 5a and d), which demonstrates the high charge storage capacitive of the NCNFs-800. Fig. 5b and e show that the capacitive contribution of the three samples increases with the scan rate.[56]

To further investigate the charge transfer resistance and cycling stability of the electrodes, electrochemical impedance spectroscopy (EIS) analysis was performed. Fig. S19a,†c displays the Nyquist plots of the NCNFs in Li$^+$/Na$^+$ half cells, for Li$^+$ half cells and Na$^+$ half cells, it is clearly observed that the charge-transfer resistance (R_{ct}) values of NCNFs-800 is lower than those of NCNFs-600 and NCNFs-700. NCNFs-800 displays a lower fitting resistance than NCNFs-600 and NCNFs-700, this demonstrates that the abundant defect structure of NCNFs-800 facilitates rapid electron transfer during the discharge/charge process.[57] Besides, the Warburg impedance Z_w is related to the diffusion process of Li$^+$/Na$^+$, which can be represented by the D value, which can be calculated using the following equations:

$$\omega = 2\pi f \tag{5}$$

$$Z' = R + \sigma\omega^{-1/2} \tag{6}$$

$$D = \frac{R^2 T^2}{2A^2 n^4 F^4 C^2 \sigma^2} \tag{7}$$

where R, T, A, n, F and σ are the ideal gas constant (8.314 J mol^{-1} K^{-1}), the absolute temperature (298 K), effective surface area of the electrode (1.5 cm^2), the number of the transferred electrons (1), the Faraday constant (96 500 C mol^{-1}), the bulk concentration (1 M) and the Warburg coefficient, respectively.[58] The Warburg coefficient (σ) can be calculated by formulas (5) and (6), as shown in Fig. S19b and d,† for Li$^+$ half cells and Na$^+$ half cells, the corresponding D_{K^+} values of NCNFs-800 is higher than NCNFs-600 and NCNFs-700, indicating that the NCNFs-800 exhibits the highest diffusion rate.[59] In addition, as shown in Fig. 5c and f, the EIS profile of the NCNFs-800 is almost overlapped after 10 cycles, indicating its good reversibility.

4. Conclusions

In conclusion, we designed a MOFs-derived strategy for nitrogen-doped porous carbon nanofibers (NCNFs) with cavities interconnected by channels, which can shorten the diffusion distances of Li$^+$/Na$^+$ and electrons and ease the volume expansion of electrode materials during cycling process. There are a large number of edge-doped nitrogen atoms on the inner surface of electrode materials, which provide many active sites for Li$^+$/Na$^+$ adsorption and improve the electrochemical performance of the material. The obtained NCNFs-800 exhibited excellent electrochemical performance with high reversible capacity (for Li$^+$ battery anodes: 1237 mA h g^{-1} at 100 mA g^{-1} after 200 cycles, for Na$^+$ battery anodes: 323 mA h g^{-1} at 100 mA g^{-1} after 150 cycles) and long-term cycling stability (or Li$^+$ battery anodes: 635 mA h g^{-1} at 2 A g^{-1} after 5000 cycles, for Na$^+$ battery anodes: 194 mA h g^{-1} at 2 A g^{-1} after 5000 cycles).

Conflicts of interest

There are no conflicts for this work to declare.

Acknowledgements

References

1 G. Huang, Q. Q. Kong, W. T. Yao and Q. Y. Wang, *J. Colloid Sci.*, 2023, **629**, 832–845.

2 X. Y. Liu, H. C. Tao, C. Y. Tang and X. L. Yang, *Chem. Eng. Sci.*, 2022, **248**, 117200.

3 K. N. Chu, X. J. Zhang, Y. Yang, Z. Q. Li, L. Z. Wei, G. Yao, F. C. Zheng and Q. W. Chen, *Carbon*, 2021, **184**, 277–286.

4 F. Xu, Y. X. Zhai, E. Zhang, Q. H. Liu, G. S. Jiang, X. S. Xu, Y. Q. Qiu, X. M. Liu, H. Q. Wang and S. Kaskel, *Angew. Chem., Int. Ed.*, 2020, **59**, 19460–19467.

5 J. F. Ruan, F. J. Mo, Z. L. Chen, M. Liu, S. Y. Zheng, R. B. Wu, F. Fang, Y. Song and D. L. Song, *Adv. Energy Mater.*, 2020, **10**, 1904045.

6 M. Chen, Y. P. Cao, C. Ma and H. Yang, *Nano Energy*, 2021, **81**, 105640.

7 Y. Liu, Y. X. Lu, Y. S. Xu, Q. S. Meng, J. C. Gao, Y. G. Sun, Y. S. Hu, B. B. Chang, C. T. Liu and A. M. Cao, *Adv. Mater.*, 2020, **32**, 2000505.

8 F. C. Zheng, Y. Yang and Q. W. Chen, *Nat. Commun.*, 2014, **5**, 5261.

9 L. Tao, Y. P. Yang, H. L. Wang, Y. L. Zheng, H. C. Hao, W. P. Song, J. Shi, M. H. Huang and D. Maitlin, *Energy Storage Mater.*, 2020, **27**, 212–225.

10 K. N. Chu, Z. Q. Li, S. K. Xu, G. Yao, Y. Xu, P. Niu and F. C. Zheng, *J. Alloys Compd.*, 2021, **854**, 157264.

11 X. T. Xu, T. Yang and Q. W. Zhang, *Chem. Eng. J.*, 2020, **390**, 124493.

12 S. T. Liu, B. B. Yang, J. S. Zhou and H. H. Song, *J. Mater. Chem. A*, 2019, **7**, 18499.

13 W. L. Zhang, J. Yin, C. L. Chen and X. Q. Qiu, *Chem. Eng. Sci.*, 2021, **241**, 116709.

14 B. Yin, S. Q. Liang, D. D. Yu, B. S. Cheng, I. L. Egun, J. D. Lin, X. F. Xie, H. Z. Shao, H. Y. He and A. Q. Pan, *Adv. Mater.*, 2021, 2100808.

15 J. Y. Mao, D. C. Niu, N. Jiang, G. Y. Jiang, M. W. Chen, Y. S. Li and J. L. Shi, *J. Mater. Chem. A*, 2020, **8**, 9768–9775.

16 S. Q. Zhao, K. Yan, J. Y. Liang, Q. H. Yuan, J. Q. Zhang, B. Sun, P. Munroe and G. X. Wang, *Adv. Funct. Mater.*, 2021, 2102060.

17 W. X. Yang, J. H. Zhou, S. Wang, Z. C. Wang, F. Lv, W. S. Zhang, W. Y. Zhang, Q. Sun and S. J. Guo, *ACS Energy Lett.*, 2020, **5**, 1653–1661.

18 R. C. Cui, B. Xu, H. J. Dong, C. C. Yang and Q. Jiang, *Adv. Sci.*, 2020, **7**, 1902547.

19 H. G. Tong, C. L. Wang, J. Lu, S. Chen, K. Yang, M. X. Huang, Q. Yuan and Q. W. Chen, *Small*, 2020, 2002771.

20 S. K. Xu, L. Cai, P. Niu, Z. Q. Li, L. Z. Wei, G. Yao, C. L. Wang, F. C. Zheng and Q. W. Chen, *Carbon*, 2021, **178**, 256–264.

21 F. C. Zheng, K. N. Chu, Y. Yang, Z. Q. Li, L. Z. Wei, Y. Xu, G. Yao and Q. W. Chen, *ACS Appl. Mater. Interfaces*, 2022, **14**, 9212–9221.

22 J. M. Chen, Y. Cheng, Q. B. Zhang, C. Luo, H. Y. Li, Y. Wu, H. H. Zhang, X. Wang, H. D. Liu, X. He, J. J. Han, D. L. Peng, M. L. Liu and M. S. Wang, *Adv. Funct. Mater.*, 2020, 2007158.

23 H. S. Yang, S. W. Kim, K. H. Kim, S. H. Yoon, M. J. Ha and J. Kang, *Appl. Sci.*, 2021, **11**, 12007.

24 Z. F. Sun, Y. X. Chen, B. J. Xi, C. Geng, W. J. Guo, Q. C. Zhuang, X. G. An, J. Liu, Z. C. Ju and S. L. Xiong, *Energy Storage Mater.*, 2022, **53**, 482–491.

25 Y. T. Chu, L. Y. Guo, B. J. Xi, Z. Y. Feng, F. F. Wu, Y. Lin, J. C. Liu, D. Sun, J. K. Feng, Y. T. Qian and S. L. Xiong, *Adv. Mater.*, 2018, **30**, 1704244.

26 L. Tao, Y. P. Yang, H. L. Wang, Y. L. Zheng, H. C. Hao, W. P. Song, J. Shi, M. H. Huang and D. Mitlin, *Energy Storage Mater.*, 2020, **27**, 212–225.

27 B. B. Fan, J. X. Yan, A. P. Hu, Z. Liu, W. Z. Li, Y. H. Li, Y. L. Xu, Y. Zhang, Q. L. Tang, X. H. Chen and J. L. Liu, *Carbon*, 2020, **164**, 1–11.

28 Y. J. Fang, X. Y. Yu and X. W. Lou, *Adv. Mater.*, 2018, **30**, 1706668.

29 L. Wang, Y. Q. Wang, M. G. Wu, Z. X. Wei, C. Y. Cui, M. L. Mao, J. T. Zhang, X. P. Han, Q. H. Liu and J. M. Ma, *Small*, 2018, **14**, 1800737.

30 Q. Y. Zhang, F. J. Liu, P. A. Gao, P. Zhao, H. X. Guo, L. Wang and Z. L. Wan, *Mater. Lett.*, 2020, **268**, 127366.

31 Q. D. Liu, F. Han, J. F. Zhou, Y. Li, L. Chen, F. Q. Zhang, D. W. Zhou, C. Ye, J. X. Yang, X. Wu and J. S. Liu, *ACS Appl. Mater. Interfaces*, 2020, **12**, 20838–20848.

32 D. P. Qiu, J. Y. Guan, M. Li, C. H. Kang, J. Y. Wei, Y. Li, Z. Y. Xie, F. Wang and R. Yang, *Adv. Funct. Mater.*, 2019, **29**, 1903496.

33 J. Wang, J. N. Liang, J. Z. Wu, C. J. Xuan, Z. X. Wu, X. Y. Guo, C. L. Lai, Y. Zhu and D. L. Wang, *J. Mater. Chem. A*, 2018, **6**, 6503–6509.

34 R. C. Cui, B. Xu, H. J. Dong, C. C. Yang and Q. Jiang, *Adv. Sci.*, 2020, **7**, 1902547.

35 J. F. Ruan, F. J. Mo, Z. Y. Long, Y. Song, F. Fang, D. L. Sun and S. Y. Zheng, *ACS Nano*, 2020, **14**, 12222–12233.

36 J. Lou, B. J. Ma, J. Peng, Z. Y. Wu, Z. G. Luo and X. Y. Wang, *ACS Sustainable Chem. Eng.*, 2019, **7**, 10415–10424.

37 C. L. Zhang, Y. Xu, G. Du, Y. H. Wu, Y. L. Li and H. P. Zhao, *Nano Energy*, 2020, **72**, 104661.

38 H. J. Xue, Z. L. Na, Y. Q. Wu, X. X. Wang, Q. Li, F. Liang, D. M. Yin, L. M. Wang and J. Ming, *J. Mater. Chem. A*, 2018, **6**, 12466–12474.

39 W. X. Yang, J. H. Zhou, S. Wang, W. Y. Zhang, Z. C. Wang, F. Lv, K. Wang, Q. Sun and S. J. Guo, *Energy Environ. Sci.*, 2019, **12**, 1605–1612.

40 X. Hu, G. B. Zhong, J. W. Li, Y. J. Liu, J. Yuan, J. X. Chen, H. B. Zhan and Z. H. Wen, *Energy Environ. Sci.*, 2020, **13**, 2431–2440.

41 J. F. Ruan, X. Wu, Y. Wang, S. Y. Zheng, D. L. Sun, Y. Song and M. Chen, *J. Mater. Chem. A*, 2019, **7**, 19305–19315.

42 Y. Liu, H. D. Dai, Y. K. An, L. J. Fu, Q. Y. An and Y. P. Wu, *J. Mater. Chem. A*, 2020, **8**, 14993–15001.

43 G. D. Park, J. K. Lee and Y. C. Kang, *Carbon*, 2018, **128**, 191–200.

44 X. X. Liu, T. Shu, L. Zhang, F. Y. Li and X. L. Hu, *Carbon*, 2019, **143**, 240–246.

45 C. Gao, J. Z. Feng, J. R. Dai, Y. Y. Pan, Y. L. Zhu, W. H. Wang, Y. F. Dong, L. F. Cao, L. Guan, L. Pan, H. Hu and M. B. Wu, *Carbon*, 2019, **153**, 372–380.

46 G. Y. Ma, C. J. Li, F. Liu, M. K. Majeed, Z. Y. Feng, Y. H. Cui, J. Yang and Y. T. Qian, *Mater. Today Energy*, 2018, **10**, 241–248.

47 W. Zhao, S. Ci, X. Hu, J. Chen and Z. Wen, *Nanoscale*, 2019, **11**, 4688–4695.

48 Y. D. Mo, Q. Ru, X. Song, S. J. Hu, L. Y. Guo and X. Q. Chen, *Electrochim. Acta*, 2015, **176**, 575–585.

49 J. Wu, X. X. Zhang, Z. Li, C. F. Yang, W. D. Zhong, W. L. Li, C. Z. Zhang, N. J. Yang, Q. Zhang and X. K. Li, *Adv. Funct. Mater.*, 2020, **30**, 2004348.

50 W. Zhong, Q. W. Chen, Z. Liu, F. Yang, W. L. Liu, K. L. Sun, F. G. Kong and M. M. Ren, *J. Alloys Compd.*, 2020, **832**, 154879.

51 F. C. Zheng, G. L. Xia, Y. Yang and Q. W. Chen, *Nanoscale*, 2015, **7**, 9637–9645.

52 P. Xue, Y. J. Zhai, N. N. Wang, Y. H. Zhang, Z. X. Lu, Y. L. Liu, Z. C. Bai, B. K. Han, G. F. Zou and S. X. Dou, *Chem. Eng. J.*, 2020, **392**, 123676.

53 Y. Li, M. H. Chen, B. Liu, Y. Zhang, X. Q. Liang and X. H. Xia, *Adv. Energy Mater.*, 2020, 2000927.

54 T. T. Wang, K. W. Yang, J. Shi, S. R. Zhou, L. W. Mi, H. P. Li and W. H. Chen, *J. Energy Chem.*, 2020, **46**, 71–77.

55 M. J. Shao, C. X. Li, T. Li, H. Zhao, W. Q. Yu, R. T. Wang, J. Zhang and L. W. Yin, *Adv. Funct. Mater.*, 2020, **30**, 2006561.

56 H. L. Deng, L. Wang, S. Y. Li, M. Zhang, T. Wang, J. Zhou, M. X. Chen, S. Chen, J. H. Cao, Q. S. Zhang, J. Zhu and B. G. Lu, *Adv. Funct. Mater.*, 2021, 2107246.

57 W. D. Li, D. Z. Wang, Z. J. Gong, X. S. Guo, J. Liu, Z. H. Zhang and G. C. Li, *Carbon*, 2020, **161**, 97–107.

58 Y. Xu, C. L. Wang, P. Niu, Z. Q. Li, L. Z. Wei, G. Yao, F. C. Zheng and Q. W. Chen, *J. Mater. Chem. A*, 2021, **9**, 16150–16159.

59 S. J. Chen, K. J. Tang, F. Song, Z. C. Liu, N. Zhang, S. L. Lan, X. Q. Xie and Z. J. Wu, *Nanotechnology*, 2022, **33**, 055401.